FULL PAPER

Suppression of Catastrophic Failure in Metallic Glass–Polyisoprene Nanolaminate Containing Nanopillars

Ju-Young Kim, Xun Gu, Matt Wraith, Jonathan T. Uhl, Karin A. Dahmen, and Julia R. Greer**

One considerable concern in metallic glass is enhancing ductility by suppressing catastrophic failure by the instantaneous propagation of shear bands. Compressed nanopillars with alternating CuZr metallic glass and polyisoprene nanolaminates exhibit >30% enhancement in plastic flow, as compared with monolithic glass, without sacrifice of strength. A suppression of stochastic strain burst signature in these metallic glass-polymer composites is reported, which is an undesirable characteristic ubiquitously present in monolithic metallic glass and in metallic glass-metal composites. The intermittent stochastic signature is quantified in each metallic glass-containing nanolaminate system by constructing histograms of burst size distributions and provide theoretical foundation for each behavior. The exceptional mechanical properties emergent in these MG-polymer nanolaminate composites are attributed to the combination of nanometer size-induced shear band suppression in metallic glasses and the damping capability of the polyisoprene layers.

1. Introduction

Metallic glasses (MGs) have shown promise in small-scale technological applications such as chemical and biological sensors and actuators, as well as in device coatings, due to their combined superior wear and corrosion resistance, metal-like electrical conductivity, and high mechanical strength and elastic limit.[1–5] However, the main hindrance preventing inserting MGs in structural applications is the absence of ductility in bulk leading to their sudden and catastrophic failure upon mechanical loads.[6–8] Considerable efforts have been geared towards eliciting and improving ductility in MGs. Among them, using reduced sample size has been reported to suppress catastrophic failure typically occurring in bulk via shear band propagation.[9–12] To date, several research groups have made strides towards understanding the effects of length scale on the deformation of MGs and on shear band formation at reduced scales mainly by conducting nanomechanical experiments. Based on these, correlations between reduced size and several mechanical attributes have been put forth: yield strength,[10–17] plasticity,[17,18] and transition from highly localized to homogeneous deformation in compression[10,12] and in tension.[9,11] While providing useful insights into small-scale MG plasticity, these experimental results are widely divergent. For example, the strengths of MG nanostructures have been reported to increase,[10,15,18,19] decrease,[12] or be independent of size.[13,14,20,21] The characteristic size for localized-to-homogeneous deformation transition has also been found to vary substantially from 400 nm[12] to 200 nm[14] and 100 nm,[9–11,22] or not observed at all down to 250 nm[21] and 150 nm.[23] These discrepancies could be due to experimental artifacts rising from imperfections in nanomechanical testing such as tapered sample geometry and loading misalignment.

Samples of different geometry to investigate size-dependent mechanical behavior of MGs with nanometer dimensions were composed of nanolaminates containing thin MG and copper (Cu) layers: 10 nm-thick PdSi MG/90 nm-thick Cu,[24] 20 nm-thick Cu_4Zr_3 MG/20nm-thick Cu,[25] and 5 nm-thick CuZr MG/35 nm-thick Cu.[26,27] These works reported the apparent ductility ranging from 3 to 15% strain, arising from the suppression of catastrophic shear band propagation. While the emergence of this enhanced deformability is a marked improvement over monolithic MGs, the ultimate tensile strengths of these nanolaminates were found to be only on the order of 1 GPa, a value closer to that of copper than of the monolithic CuZr MG due to the relatively low volume fraction of the latter. More recently, tensile behavior of micrometer-sized samples containing nanolaminates with alternating layers of 16–900 nm-thick $Cu_{50}Zr_{50}$ MG and 16 nm-thick nanocrystalline-copper (nc-Cu) with interfaces oriented parallel to the deformation was reported.[22] In these experiments, the 25% improvement in ultimate tensile strength was accompanied by only a marginal fracture strain enhancement of 4% for samples

Prof. J.-Y. Kim
School of Mechanical and Advanced Materials Engineering
UNIST, Ulsan 689-798, Korea
E-mail: juyoung@unist.ac.kr
X. Gu, Prof. J. R. Greer
Department of Applied Physics and Materials Science
California Institute of Technology
Pasadena, CA 91125, USA
E-mail: jrgreer@caltech.edu
M. Wraith, J. T. Uhl, Prof. K. A. Dahmen
Department of Physics
University of Illinois at Urbana-Champaign
Urbana, IL 61801, USA

DOI: 10.1002/adfm.201103050

with the critical MG layer thickness below 120 nm.[22] Therefore, the challenge remains to develop MG-containing nanolaminate composites, which would exhibit strengths as high as monolithic MGs while being capable of metal-like ductility.

Here we report enhanced plastic flow of greater than 30% attained by nanolaminate-containing samples with alternating layers of $Cu_{50}Zr_{50}$ MG and polyisoprene at flow stresses comparable to compressive strengths of 400 nm-diameter pure $Cu_{50}Zr_{50}$ MG nanopillars. Further, we demonstrate the suppression of stochastic strain bursts in these MG-polymer composites, an undesirable characteristic ubiquitously present in monolithic MGs and in MG-metal composites. We explain these unique emergent properties in the framework of size-dependent MG deformation, polymer-induced shear band propagation suppression and provide statistical analysis of strain burst distributions for each material system.

2. Material Systems

We designed and synthesized nanolaminates with alternating layers of 100 nm-thick $Cu_{50}Zr_{50}$ MG and 19 nm-thick polyisoprene, which we label as "material system 3" or "MS 3" hereafter for convenience, as shown in **Figure 1**c. We also prepared three additional types of samples for comparison: 1) pure $Cu_{50}Zr_{50}$ MG, hereafter referred to as material system 1 (MS 1), shown in Figure 1a; 2) nanolaminates with alternating layers of 112 nm-thick $Cu_{50}Zr_{50}$ MG and 16 nm-thick nanocrystalline-Cu with ≈16 nm grain sizes, material system 2 (MS2), shown in Figure 1b; and 3) nanolaminates with alternating layers of 166 nm-thick $Cu_{50}Zr_{50}$ MG and 19n m-thick polyisoprene, material system 4 (MS 4), shown in Figure 1d. Nanopillars with diameters of ≈400 nm and heights of ≈950 nm were prepared from each set of these material systems by focused ion beam (FIB) fabrication via the top-down technique,[28–30] resulting in the pillar axes oriented orthogonally to interfaces. An inevitable consequence of utilizing this top-down FIB fabrication procedure is that all nanopillars have a small amount of vertical taper, on the order of ≈3°. However, in these structures the top-down FIB fabrication has clear merits since it minimizes FIB-induced surface damage in MG layers, affecting only the outer rim of the disc-shaped MG layers, because only the sidewalls of the nanopillars are exposed to the ion beam at the glancing angle. Notably, despite the identical nanopillar diameters, the critical dimension for shear banding in monolithic MG samples is the entire pillar height (≈950 nm)[12] while that in the nanolaminates pillars is the thickness of the MG layers: 100 nm and 166 nm in the nanolaminates with polyisoprene and 112 nm in the nanolaminates with nanocrystalline-copper (nc-Cu).

3. Results and Discussion

Figure 2 shows engineering stress–strain curves for the nanopillar compressions from each set of these four material systems. At least five reproducible stress–strain curves for each

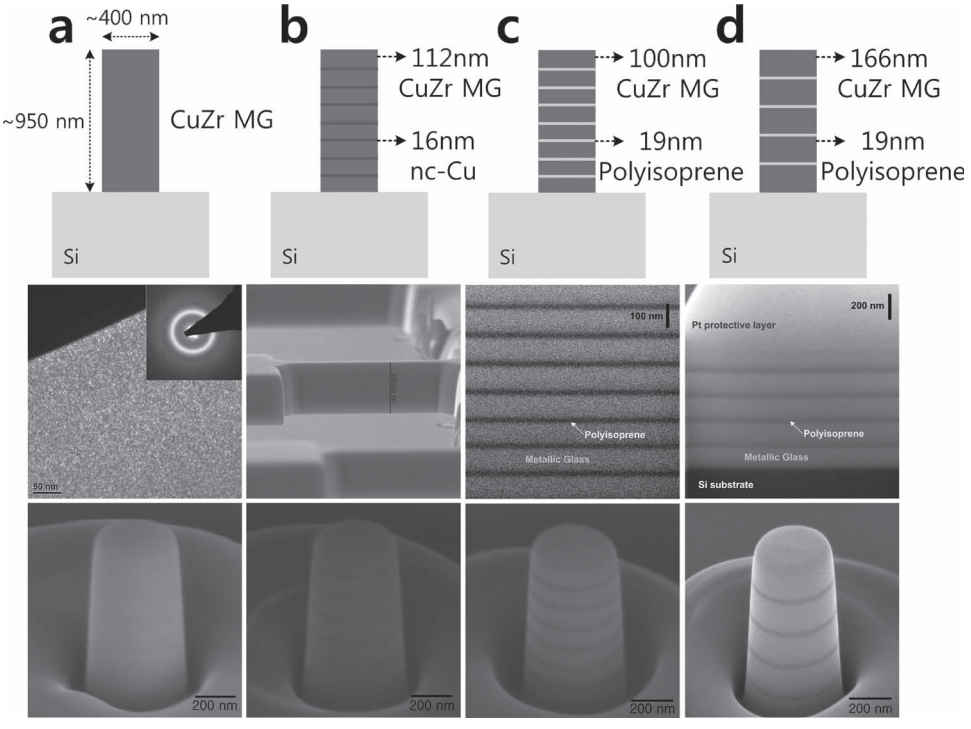

Figure 1. Schematics, scanning electron microscopy (SEM), and bright-field transmission electron microscopy (TEM) images of nanolaminate stack cross-sections and SEM images of nanopillars for a) MS 1, pure CuZr MG; b) MS 2, nanolaminates with alternating layers of 112 nm-thick CuZr MG and 16 nm-thick nanocrystalline-Cu; c) MS 3, nanolaminates with alternating layers of 100 nm-thick CuZr MG and 19 nm-thick polyisoprene; and d) MS 4, nanolaminates with alternating layers of 166 nm-thick CuZr MG and 19 nm-thick polyisoprene.

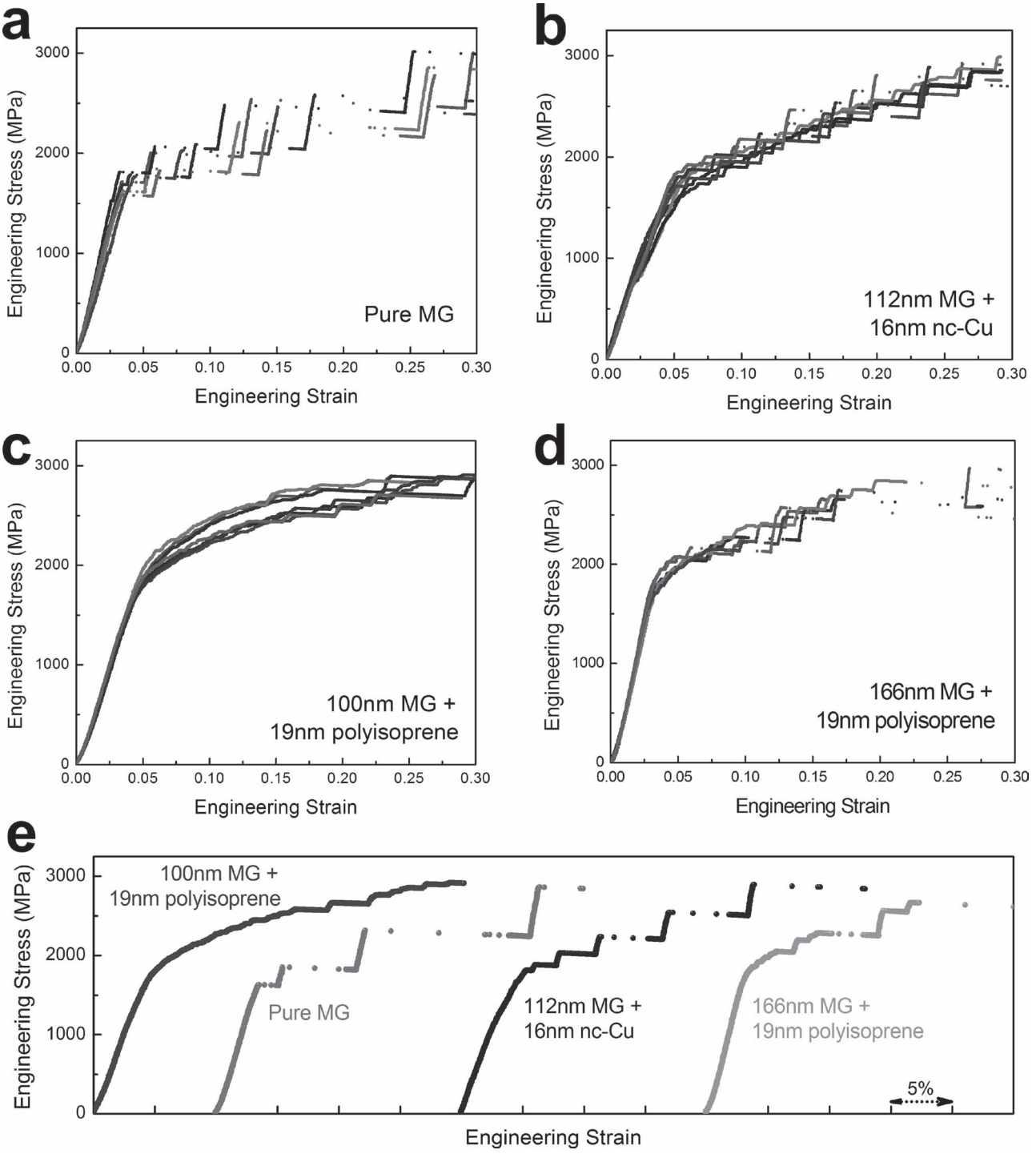

Figure 2. Compressive engineering stress–strain curves of a) MS 1, pure CuZr MG; b) MS 2, nanolaminates with alternating layers of 112 nm-thick CuZr MG and 16 nm-thick nanocrystalline-Cu; c) MS 3, nanolaminates with alternating layers of 100 nm-thick CuZr MG and 19 nm-thick polyisoprene; and d) MS 4, nanolaminates with alternating layers of 166 nm-thick CuZr MG and 19 nm-thick polyisoprene. e) Individual typical engineering stress–strain curves for each system provided for intersystem comparison.

sample were used to analyze mechanical and statistical data. In addition, individual typical curves from each material system are plotted in Figure 2e for comparison. A set of compressive stress–strain curves of MS1, monolithic 400 nm-diameter MG nanopillars, is shown in Figure 2a, revealing that they are composed of intermittent elastic loadings and pronounced discrete strain bursts, a behavior typical of MGs deforming at room temperature.[10,31] Relatively short strain bursts initiated at ≈3% strain immediately upon yielding likely correspond to the formation and propagation of diffuse shear bands from the

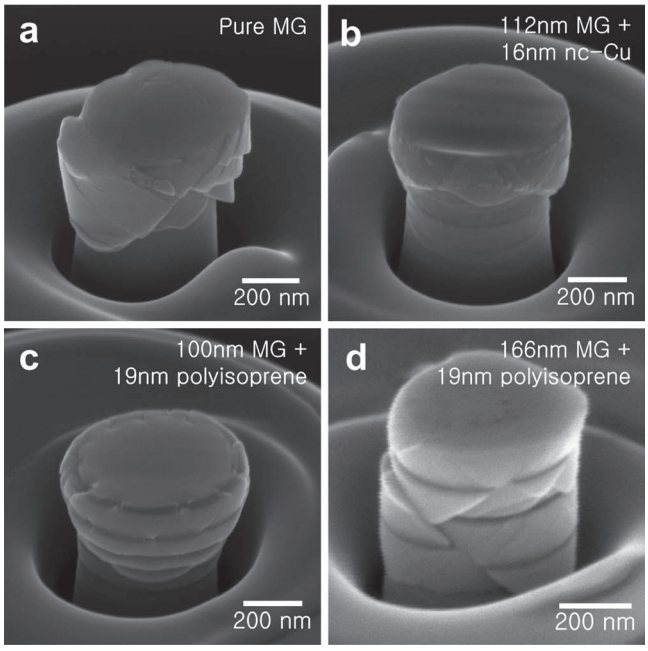

Figure 3. SEM images of nanopillars after compression for a) MS 1, pure CuZr MG; b) MS 2, nanolaminates with alternating layers of 112 nm-thick CuZr MG and 16 nm-thick nanocrystalline-Cu; c) MS 3, nanolaminates with alternating layers of 100 nm-thick CuZr MG and 19nm-thick polyisoprene; and d) MS 4, nanolaminates with alternating layers of 166 nm-thick CuZr MG and 19 nm-thick polyisoprene. All images were taken at 52° tilt angle.

tops of the nanopillars since local stress concentrations arise in those locations due to tapered geometry. These bursts become longer after ≈5% strain and are indicative of the shear bands passing through the entire nanopillar volume. The stress-strain curves are characterized by segments of elastic loadings leading to ever-higher stresses, which activate shear banding events, followed by rapid, discrete bursts. In contrast to the plastic flow of crystalline metals, whereby more severe deformation leads to defect accumulation and causes strain-hardening, in small-scale MG deformation, elastically stored energy is released during the discrete bursts, which weakens their subsequent elastic energy storage capability. This type of deformation is highly unpredictable, rendering the insertion of MGs into structural applications impractical. **Figure 3** shows typical SEM images of nanopillars from each material system after compression to the maximum strain of 35% or higher, with Figure 3a displaying multiple shear bands emanating from the monolithic MG pillar top.

Deformation of the 2nd material system (MS2)–nanolaminates with alternating layers of 112 nm-thick MG and 16 nm-thick nc-Cu, shown in Figure 2b, is also characterized by discrete strain bursts, although seemingly of shorter extent, and exhibit steep strain-hardening up to ≈5% strain after 2.33% ± 0.25% yield strain. This result indicates that introduction of nc-Cu layers improves plasticity in the nanolaminates over monolithic MGs of the same dimensions up to ≈5% strain, as revealed by stable strain hardening and non-catastrophic bursts. Interestingly, this occurrence of shorter strain bursts is in contrast to the work of Liu et al.,[32] who observed a stress–strain signature with a serrated flow typical of monolithic MGs in their CuZr/Zr nanolaminates. This distinction likely arises from the different layer thicknesses of 570 nm used in their work, which is larger than the critical brittle-to-ductile transition thickness identified in our previous work on the same system.[22] Figure 3b shows suppression of shear band formation in MG layers as they do not contain long shear bands throughout the entire nanopillar volume with sharp surface steps unlike pure MG nanopillars shown in Figure 2a. Examining each MG layer closer reveals that shear bands did not propagate, but rather the deformation can be described as "bulbous," whereby the structure deformed by widening out in the top half, forming scalloped sidewalls.

In contrast to MS 1 and 2, the 3rd material system (MS3) containing nanolaminates with alternating layers of 100 nm-thick MG and 19 nm-thick polyisoprene, as shown in Figure 2c, clearly shows almost continuous strain-hardening. Plasticity here commences in a much smoother fashion than other systems in this study up to ≈15% strain. At higher strains, the load frequently drops, albeit much slower than during discrete bursts in other systems. We used data acquisition rate of 25 Hz for all compressions, so the time elapsed during each burst is directly related to the number of data points captured in it. The SEM image of these post-mortem samples shown in Figure 3c clearly reveals the lack of shear bands, favoring a bulbous shape with scalloped sidewalls that is even more pronounced than in MS2.

To test whether this shift towards bulbous morphology over shear banding is due to the dampening effect of the thin polymer layer or to the size-dependent MG behavior at the nanoscale, we fabricated a fourth material system (MS4), nanolaminates containing 166 nm-thick MG and 19 nm-thick polyisoprene layers. Note that this MG thickness is well above any brittle-to-ductile size reported previously[22] and, therefore, is expected to deform via fully propagated mature shear bands. In contrast to the thinner MG-polymer nanolaminates, the compressive stress–strain curves corresponding to this thicker MG-polymer system, shown in Figure 2d, are unambiguously composed of intermittent strain bursts. The strain bursts likely correspond to fully activated shear bands cutting through the polyisoprene layers without interruption and leading to the formation of shear offsets throughout the entire nanopillar volume, as clearly shown in Figure 3d. This signature is nearly identical to that of pure MG nanopillar deformation shown in Figure 3a rather than to the bulging morphologies of MS2 and 3. Also, while we observe marginal extension along the in-plane direction in thinner MG-polymer nanolaminates, these thicker MG/polyisoprene systems clearly deform by shear band formation only rather than via in-plane extension.

Table 1 summarizes the yield strengths of samples from each of the four material systems measured by 0.2% offset method.

Table 1. Yield strength and maximum attained flow stress at ≈30% strain for four material systems.

Material system	1 pure MG	2112 nm MG/16 nm nc-Cu	3100 nm MG/19 nm polyisoprene	4166 nm MG/19 nm polyisoprene
Yield strength [MPa]	1526.2 ± 87.9	870.4 ± 103.1	1563.6 ± 69.6	1676.6 ± 65.39
Maximum flow stress at ≈30% strain [MPa]	2777.8 ± 22.3	2838.0 ± 60.9	2859.3 ± 76.5	2753.2 ± 155.0

Remarkably, it appears that despite the distinct differences in their structural and chemical constituents, the yield strengths of all samples with the exception of MG/nc-Cu samples fall within one standard deviation range of one another. The lower yield strength of MG-nc-Cu system can be explained by plasticity initiating in the Cu layers rather than in the MG, with the yield strength of 870.4 ± 103.1 MPa agreeing well with that evaluated by a nanomechanical model in previous work.[22] Since the strength of polyisoprene is generally very low, on the order of 1 MPa,[33] the polymer does not contribute to the nanolaminates strength and likely serves as a damping layer during nanolaminate deformation. It is, therefore, perplexing, that the yield strengths of all MG-polyisoprene containing nanolaminates are independent of their thicknesses despite the change in deformation mode at the critical MG thickness of ≈120 nm. As mentioned above, experimental reports on size effect in MGs are dispersal and controversial. Likening shear band propagation to crack-like phenomena by utilizing Griffith's theory, Spaepen et al. proposed the following relation: $\sigma = \sqrt{\frac{2\sqrt{2}\Gamma E}{ad}}$, where Γ is the shear band energy density per unit area, E is Young's modulus, and a and d are aspect ratio and diameter, respectively.[9,11,12] Note that their product is simply the length (or height) of the deforming gauge section for pillar-like geometries. By varying MG layer thickness from 950 nm in monolithic samples to 166 nm and 100 nm in the nanolaminates samples, we vary the aspect ratio of each MG layer in the above equation, thereby testing the hypothesis that if shear banding were akin to crack propagation, the yield strength of the nanolaminates should vary inversely with the deforming gauge length, here the MG layer thickness. The Griffith theory only applies to those cases where shear bands form, hence it is only applicable to MS1 and MS4 in our study. Our findings, however, reveal that the polymer-MG nanolaminates of all thicknesses, as well as monolithic MG nanopillars, yield at nearly identical stresses, suggesting that additional kinetic mechanisms likely contribute to yielding.

We also analyzed the maximum attained strengths at ≈30% compressive strains, summarized in Table 1, and found them to be nearly identical as well. This is possibly because during uniaxial compression experiments, each layer in the nanolaminates is under an iso-stress condition, so the measured strength is simply that of the MG constituents. Though there is some variation in the maximum strengths attained by these four material systems, they also appear to be within one standard deviation of one another, further implying that the maximum attained stress in the MG-containing nanolaminates and in monolithic MG samples is independent the transition in deformation mode.

To quantify the differences among the intermittent deformations characteristics in the 4 tested material systems we obtain histograms of slip-avalanche sizes from the displacement versus time data. We define the start of a strain-burst or slip avalanche as the time when the displacement rate is larger than the applied driving rate since all experiments were conducted at a constant displacement rate. The end of an event is defined as the point where displacement rate drops back to below this threshold value. We take the difference between the initial and final displacements of such an event to define the slip size of an avalanche.

Figure 4 shows the corresponding complementary cumulative histograms of slip-avalanche sizes. We find two types of distributions: type 1 (called "PL" in **Figure 5**) corresponds to histograms with mostly small slip events that are exponentially distributed and type 2 histograms (called "QP" in Figure 5) are characterized by much larger slips, corresponding to the propagation of fully mature shear bands in addition to the small events. The type of distribution appears to be a strong function of the ratio of polyisoprene versus MG thickness. These distributions clearly convey that the monolithic CuZr MG nanopillars (MS1) are effectively more "homogeneous" relative to the other three types of pillars because they are uniformly made of the same material (see Figure 4a). As a result they show some of the largest strain bursts compared to the other types of pillars: the sizes of the relatively small strain bursts in their stress–strain curves are exponentially distributed. At higher compressive strains, shear bands form, causing more extensive slips that span the entire pillar cross-section. Each experiment on the monolithic pillars may have four or five such large events before failure, but they are all of the same order of magnitude, likely defined by the pillar size. In contrast, Figure 4b,c show that most polyisoprene-layered pillars deform almost continuously, with slips of negligible size. Some of these samples also appear to contain few larger events, but none as large as observed in the monolithic MG pillars (MS1). Figure 4d shows that most copper-layered pillars, but not all, experience some large events. Based on these distributions, it is evident that the monolithic pillars experience the largest events, the polyisoprene-layered pillars experience the smallest, and the copper-layered pillars are in between. This implies that in the nanolaminates-containing pillars the shear bands either do not form at all or form but propagate only very short distances as they become arrested by the surrounding layers. Increasing the thickness of the MG layers relative to the polyisoprene layers seems to facilitate more large events: in Figure 4c the CuZr layers are 1.6 times larger than in the samples shown in Figure 4b. The slip size distributions of some samples in Figure 4c extend to much larger slips than those in Figure 4b. This can be understood by noting that increasing the MG layer thickness effectively increases the regions of brittle material in the system, allowing shear bands to form and propagate.

We demonstrate that the simple analytical model of ref.[34–36] can be used to explain these histograms and their dependence on the sample properties. This model assumes that the MG has weak spots, which slip if the stress in their vicinity exceeds a local failure stress and then re-stick. This type of framework is relevant for MGs since their plasticity commences by localized shear events within the so-called shear transformation zones (STZs). Elastic coupling of the slips triggers other weak spots to also slip, and this cascade of slips results in an avalanche, or a "strain-burst". After a spot slips, its local failure threshold is weakened by an amount proportional to the "weakening parameter" ε until the slip avalanche is completed. This weakening is effectively related to the coalescence of individual STZs into mature shear bands, and therefore to the MG's susceptibility to catastrophic shear band formation. After the completion of a slip avalanche all thresholds re-heal back to their original value.[34]

In detail, each site in the system has an associated failure stress τ_f. If the local shear stress exceeds this failure stress then

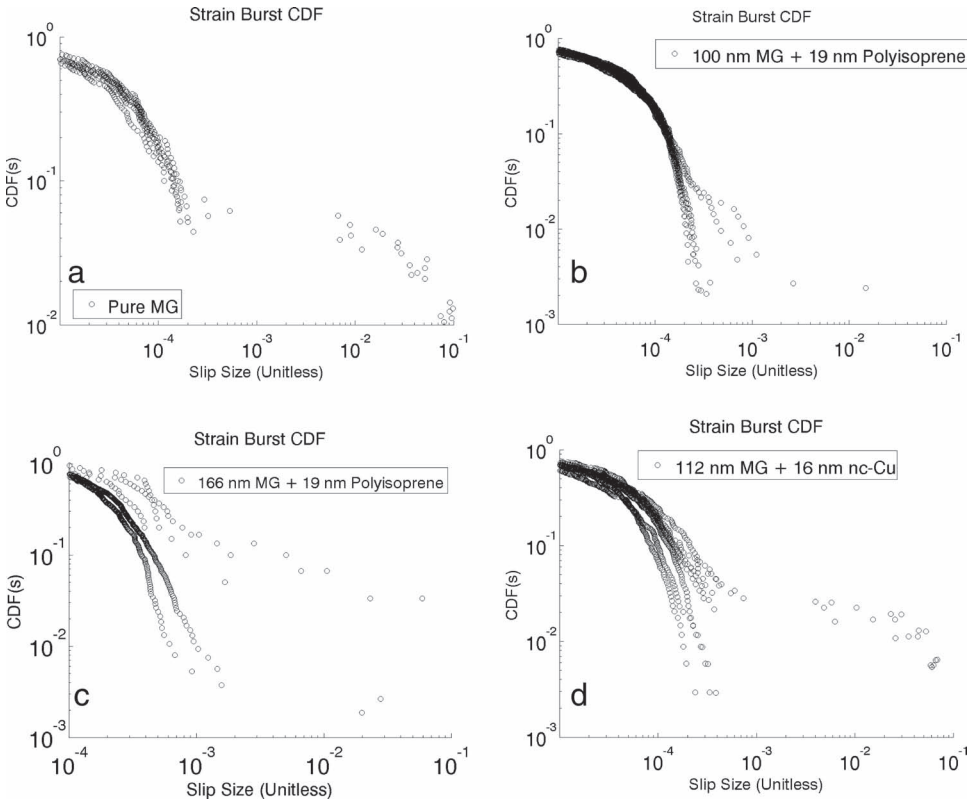

Figure 4. a) Log–log plot of the complementary cumulative distribution function (CDF) for the slip sizes for monolithic of CuZr MG nanopillars. Note that every experiment has some large slip-events. b) CDF for 7 pillars with 100 nm-thick CuZr layers and 19 nm-thick polyisoprene layers. 2 out of 7 experiments contain large events. c) Similar experiment as in (b) except the layers of CuZr are 166 nm thick. The large events are larger than in (b), as is expected from the model. Some samples show only small events, as in (b). d) 5 out of 8 experiments contain large events for a pillar with 112 nm CuZr metal glass layers separated by 16 nm nanocrystalline Cu layers. Samples in (a,b,d) are all roughly 400 nm in diameter and roughly 950 nm in length. Samples in (c) are all roughly 440 nm in diameter and roughly 1 micrometer in length.

the site slips till its local stress drops down to a local arrest stress τ_a. Both τ_f and τ_a can be picked from a random distribution to model the disorder in the MG. The statistics of the slip avalanches has been shown to only depend on the difference between those stresses, so that it suffices to assign random values (chosen from an appropriate probability distribution) to either τ_f or τ_a and keep the other a constant throughout the sample.[34] If there is weakening, and if a site has slipped once during an ongoing slip-avalanche, then its local threshold is immediately reduced to a lower dynamic value, τ_d. Its threshold remains at the weakened value τ_d until the slip avalanche is completed. The weakening parameter ε is then defined as $\varepsilon = (\tau_d - \tau_a)/(\tau_f - \tau_a)$. At the end of a slip avalanche the weakened sites reheals back to their static threshold strength τ_f.[34] Elastic coupling redistributes the stress that is released during a local slip event $\Delta\tau_{released} = (\tau_f - \tau_a)$ or $\Delta\tau_{released} = (\tau_d - \tau_a)$ to the other sites in the system.

In the case of monolithic MGs (i.e., in the absence of layers of other materials) the model predicts slip avalanche distributions of type 2, as shown in **Figure 6**a, similar to those seen in experiments on monolithic MGs (Figure 4a). The distribution of slip sizes S of the small events can be written in the form $D(S) \approx S^{-3/2} F(S\varepsilon^2)$. Here F is an exponentially decaying scaling function, which cuts off the avalanche size distribution near $S_{max} \approx 1/\varepsilon^2$. For example, the small event regime in Figure 6a,d decays exponentially, as predicted by this expression. In addition the model predicts almost periodically recurrning much larger, system-spanning slip events, that are also visible in the same plots.

For polyisoprene-layered samples, some of the stress released in the MG as a result of the slips is absorbed by the polyisoprene layers, so that only a fraction $\delta\tau_{MG} = c\delta\tau_{released}$ of the stress $\delta\tau_{released}$ that is released during a local slip is redistributed among the polymer and the remaining MG layers. Our model captures this situation with a reduced stress-conservation parameter, c, which is equal to the ratio $c = \delta\tau_{MG}/\delta\tau_{released}$ of the stress that is redistributed to the MG layers to stress $\delta\tau_{released}$ that is released during a local slip. In the absence of polyisoprene layers the material is modeled by $c = 1$, which means that all released stress is fully redistributed to the MG. MG systems with polyisoprene layers, however, are effectively modeled by $c < 1$, because only the fraction c of the released stress is redistributed to the MG. The remaining fraction $(1 - c)$ is "dissipated" via deformation of the polyisoprene layers. Systems with very thick polyisoprene layers (relative to the MG layers) are modeled by $c \ll 1$, because most of the stress will be

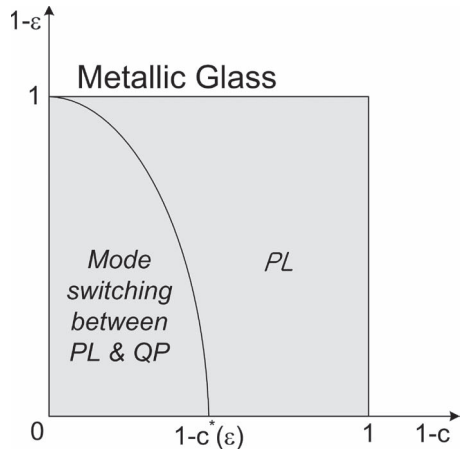

Figure 5. Dynamic phase diagram of the model in ref. [31]. The curved line indicates a phase boundary $1 - c*(\varepsilon)$. For $\varepsilon > 0$ and $1 - c < 1 - c*(\varepsilon)$ the model predicts mode switching between time periods with power law slip-size distributions with an exponential cutoff (PL), as seen in Figure 6b,c, and time periods that also have almost ("quasi") periodically recurring much larger slips (QP), as seen in Figure 6a,d.

absorbed by the polyisoprene layers. In other words, c decreases with increasing relative polymer layer thickness because more stress is absorbed by the layering material. The nanocrystalline copper layers appear to have a similar effect as well. For c close to 1 and ε close to 0 the predicted slip avalanche size distribution may be of type 1 or type 2, depending the precise parameter values. The distribution of small events (i.e., those that do not span the entire pillar) scales as: $D(S) \approx 1/S^{\frac{3}{2}} F'(S\varepsilon^2, \varepsilon/C)$, where F' is another exponentially decaying scaling function, which reduces to $F(S\varepsilon^2)$ for $c = 1$. For sufficiently small c the avalanche size distribution is of type 1: the large system spanning events seen for $c = 1$ and and $\varepsilon > 0$ are broken up into small events and the distribution of slip sizes looks essentially power-law distributed over a narrow range with a small exponential cutoff, as seen for example in Figure 6c (see ref. [34–36]). This corresponds to the regime marked "PL" in the dynamical phase diagram of Figure 5. Figure 6a–d shows the corresponding slip avalanche size distributions for simulations of the model for different c and ε parameters, effectively corresponding to different polymer or copper layer thicknesses in the experiments of Figure 4a–d. Remarkably, the simulation results in Figure 6a–d strongly resemble the corresponding experimental results of Figure 4a–d. Significantly, the correspondence is consistent with the above explanation that the layering materials absorb a fraction $1 - c$ of the redistributed stress, where $1 - c$ is grows monotonically with the thickness of the polyisoprene layers: Figure 4a,d shows statistics for samples without polyisoprene layers. Comparison with Figure 6a,d shows that the model statistics for c close to

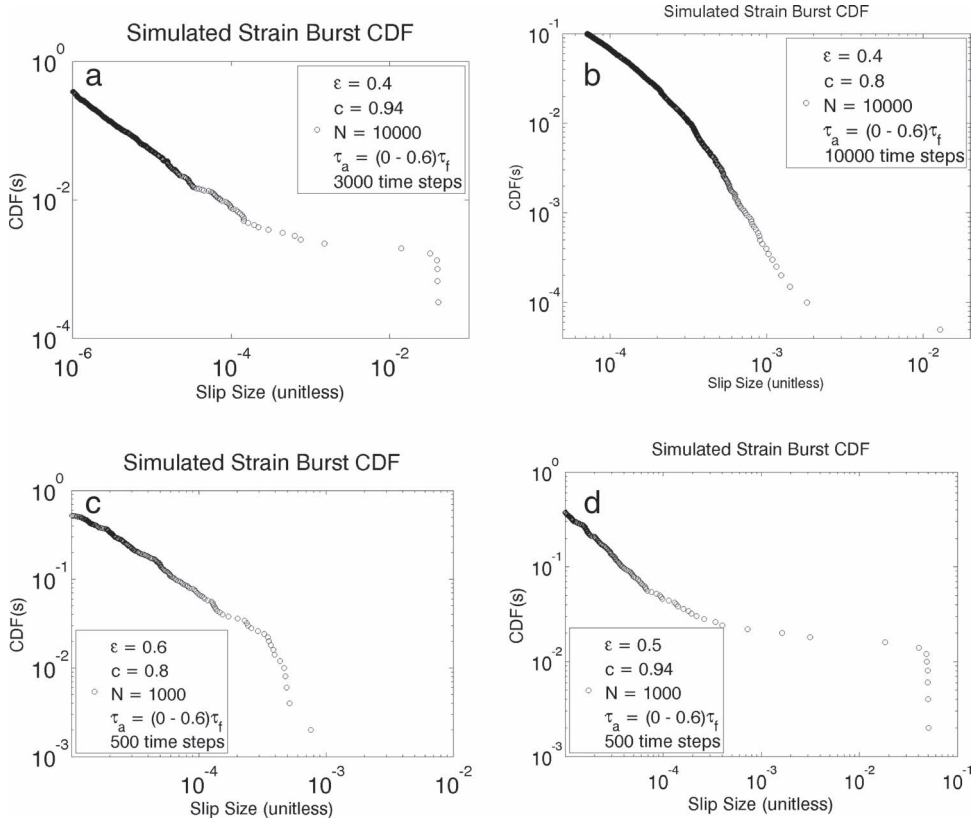

Figure 6. a–d) CDFs of slip-size distributions from simulations of the simple model of ref. [31] for different values of the weakening parameter ε and stress conservation parameter c, for different system sizes N, different total numbers of avalanches (time steps), and for different widths of distributions of arrest stresses τ_a relative to the failure stress τ_f. The parameter values for each plot are shown in the legends. Note that the slip-size distributions strongly resemble the experimental CDFs in Figure 4 (see text).

1 look indeed very similar to the experimental results for these samples. Similarly, the samples of Figure 4b,d contain 19 nm thick polyisoprene layers. Their slip statistics strongly resemble those obtained from the model for a much smaller value of c (c = 0.8) in the simulations, as expected from the above argument.

For some parameter regimes the experiments show that different samples with the same parameters can lead to histograms of type 1 ("PL") or 2 ("QP"), presumably depending on the initial local stress distribution within the MG (see for example Figure 4c). The same is also true for the model. The phase diagram in ref. [34–36] shows that for a certain range of c and ε the model shows mode switching between slip-size histograms of 1 ("PL") and type 2 ("QP") (see Figure 5). During our compression experiments only a relatively small overall number of slips can be observed due to the limited sample size. Therefore, each sample displays either a type 1 or type 2 slip size histogram, without switching into the other mode during the short observation time. Which histogram is observed for each sample depends on the initial conditions of the initial stresses and the amount of disorder in the sample.[34–36] The probability with which each histogram is observed depends on the parameters c, N, and ε in the model. In the real system that corresponds to dependence on the polymer/Cu thickness, relative to the thickness of the MG, the pillar size, and on the susceptibility to breaking of the MG, respectively.

4. Conclusions

We demonstrate fabrication methodology and mechanical properties of nanolaminates-containing nanopillars where one constituent is a $Cu_{50}Zr_{50}$ MG (MG). Specifically, we report the enhanced mechanical properties of such MG-containing nanolaminates and provide useful guidelines for utilizing these composites in structural design. Total of four distinct systems were tested: pure MG; nanolaminates with 112 nm-thick MG and 16nm-thick nanocrystalline-Cu; nanolaminates with 100 nm-thick MG and 19 nm-thick polyisoprene; and nanolaminates with 166 nm-thick MG and 19 nm-thick polyisoprene. We find that the deformation shifts from localized, shear-band dominated to relatively homogeneous, characterized by mushrooming and bulging when the MG thickness is reduced below 120 nm. Despite this transition in the deformation mode, these samples exhibit nearly identical yield strengths and flow stresses, suggesting that strength and deformation mode are decoupled from one another in these nanolaminates systems. Finally, we show a systematic suppression of discrete strain bursts ubiquitously present in the stress–strain curves of nanopillars by adding a thin polyisoprene constituent to the nanolaminates with alternating MG layers with thicknesses at or below ≈120 nm. The complementary cumulative histograms of slip-avalanche sizes constructed based on our experimental data for each material systems appear to agree with a mean-field analytical theory, also predicting the same trends. We attribute these exceptional mechanical properties to the combination of size-induced shear band suppression in MGs below a critical nanoscale thickness and the damping role of the polymer layers. Compared with both monolithic MGs and nanocomposites containing MGs and crystalline metals, our MG-polyisoprene nanolaminates retain the merits of polyisoprene such as hydrophobicity and damping capabilities while concurrently gaining exceptional strength of MGs. Our findings may provide a useful foundation for the application of these types of nanolaminates into nanodevices and structural applications requiring harsh wear and corrosion resistance and robust structural performance, as well as understanding the fundamental scientific principles driving post-elastic deformation in MG-based nanocomposite systems.

5. Experimental Section

$Cu_{50}Zr_{50}$ MG layers were deposited in a radio frequency (RF) magnetron sputtering system manufactured by AJA International, Inc. (MA, USA) from separate pure Cu and Zr targets with RF power of 56 W and 224 W, respectively. Nanocrystalline Cu layers were deposited from a pure Cu target with RF power of 102 W. Base pressure was 2.10^{-7} Torr or lower and processing pressure was 3 mTorr of Ar gas. The composition of $Cu_{50}Zr_{50}$ MG was confirmed by energy dispersive X-ray spectroscopy (EDS). It was also confirmed that the variation in the composition was negligible over the area of 2.2 cm^2 at the center of sample stage in the sputter and samples sputtered only in this area were used to minimize positional variation in composition. During processing, a 950 nm-thick film of pure MG was first deposited on a (100) silicon wafer with 4 in. diameter. Nanolaminates with alternating layers of $Cu_{50}Zr_{50}$ MG and nanocrystalline Cu were deposited by alternating the targets without breaking the vacuum. For polymer-containing systems, polyisoprene layers were spin-coated onto the appropriate layers. A solution of 1 wt% polyisoprene in xylene was prepared and 19 nm thick polyisoprene layers were coated on MG layers at the spin rate of 4000 rpm. Samples were transferred to the sputtering chamber immediately after the spin-coating and remained in the chamber for at least 30 min in order to dry before sputtering the subsequent MG layers. After preparing these multilayered thin films, nanopillars with diameters of ≈400 nm and heights of ≈950 nm were etched using a focused ion beam (FIB) (Nova 200 NanoLab, FEI Co., Hillsboro, OR, USA). The nanopillars were subsequently compressed in the DCM module of Nanoindenter G200 (Agilent Corp., Santa Clara, CA, USA) with a 8 μm diameter FIB-machined diamond flat punch tip, at a constant nominal displacement rate of 1 nm s^{-1}. Engineering stresses and strains were computed by using initial geometry of the pillars as obtained from SEM images.

Acknowledgements

The authors gratefully acknowledge the financial support of the Defense Advanced Research Projects Agency through J.R.G.'s Young Faculty Award (grant no. N66001-09-1-2092), the United Technologies Research Center post-doctoral fellowship program at Caltech, and critical support and infrastructure provided by the Kavli Nanoscience Institute (KNI) at Caltech. J.Y.K. and J.R.G. thank Robert Maass and Dongchan Jang for useful discussion and taking TEM images. K.D. and M.W. thank Braden Brinkman, Nir Friedman, Michael LeBlanc, and Georgios Tsekenis for helpful conversations and gratefully acknowledge support from NSF via DMR 10-05209.

Received: December 16, 2011
Published online: February 15, 2012

[1] A. L. Greer, *Science* **1995**, *267*, 1947.
[2] A. L. Greer, E. Ma, *MRS Bull.* **2007**, *32*, 611.
[3] W. L. Johnson, *MRS Bull.* **1999**, *24*, 42.
[4] F. Spaepen, *Acta Metall.* **1977**, *25*, 407.
[5] W. H. Wang, C. Dong, C. H. Shek, *Mater. Sci. Eng. R.* **2004**, *44*, 45.
[6] R. Maaß, D. Klaumünzer, J. F. Löffler, *Acta Mater.* **2011**, *59*, 3205.

[7] R. Maaß, D. Klaumünzer, E. I. Preiß, P. M. Derlet, J. F. Löffler, *Scripta Mater.* **2012**, *66*, 231.
[8] P. Poulopoulos, S. Baskoutas, L. F. Kiss, L. Bujdosó, T. Kemény, F. Wilhelm, A. Rogalev, V. Kapaklis, C. Politis, M. Angelakeris, K. Saksl, *J. Non-Cryst. Solids* **2008**, *354*, 587.
[9] H. Guo, P. F. Yan, Y. B. Wang, J. Tan, Z. F. Zhang, M. L. Sui, E. Ma, *Nat. Mater.* **2007**, *6*, 735.
[10] D. Jang, C. T. Gross, J. R. Greer, *Int. J. Plast.* **2011**, *27*, 858.
[11] D. C. Jang, J. R. Greer, *Nat. Mater.* **2010**, *9*, 215.
[12] C. A. Volkert, A. Donohue, F. Spaepen, *J. Appl. Phys.* **2008**, *103*, 083539.
[13] C. Q. Chen, Y. T. Pei, J. T. M. De Hosson, *Philos. Mag. Lett.* **2009**, *89*, 633.
[14] C. Q. Chen, Y. T. Pei, O. Kuzmin, Z. F. Zhang, E. Ma, J. T. M. De Hosson, *Phys. Rev. B* **2011**, *83*, 180201.
[15] Y. H. Lai, C. J. Lee, Y. T. Cheng, H. S. Chou, H. M. Chen, X. H. Du, C. I. Chang, J. C. Huang, S. R. Jian, J. S. C. Jang, T. G. Nieh, *Scripta Mater.* **2008**, *58*, 890.
[16] B. E. Schuster, Q. Wei, M. H. Ervin, S. O. Hruszkewycz, M. K. Miller, T. C. Hufnagel, K. T. Ramesh, *Scripta Mater.* **2007**, *57*, 517.
[17] Z. W. Shan, J. Li, Y. Q. Cheng, A. M. Minor, S. A. S. Asif, O. L. Warren, E. Ma, *Phys. Rev. B* **2008**, *77*, 155419.
[18] S. Cheng, X. L. Wang, H. Choo, P. K. Liaw, *Appl. Phys. Lett.* **2007**, *91*, 201917.
[19] C. J. Lee, J. C. Huang, T. G. Nieh, *Appl. Phys. Lett.* **2007**, *91*, 161913.
[20] A. Dubach, R. Raghavan, J. F. Loffler, J. Michler, U. Ramamurty, *Scripta Mater.* **2009**, *60*, 567.
[21] B. E. Schuster, Q. Wei, T. C. Hufnagel, K. T. Ramesh, *Acta Mater.* **2008**, *56*, 5091.
[22] J.-Y. Kim, D. Jang, J. R. Greer, *Adv. Funct. Mater.* **2011**, *21*, 4550.
[23] X. L. Wu, Y. Z. Guo, Q. Wei, W. H. Wang, *Acta Mater.* **2009**, *57*, 3562.
[24] A. Donohue, F. Spaepen, R. G. Hoagland, A. Misra, *Appl. Phys. Lett.* **2007**, *91*, 241905.
[25] T. G. Nieh, T. W. Barbee, J. Wadsworth, *Scripta Mater.* **1999**, *41*, 929.
[26] Y. M. Wang, A. V. Hamza, T. W. Barbee, *Appl. Phys. Lett.* **2007**, *91* , 061924.
[27] Y. M. Wang, J. Li, A. V. Hamza, T. W. Barbee, *Proc. Natl. Acad. Sci. USA* **2007**, *104*, 11155.
[28] S. Brinckmann, J. Y. Kim, J. R. Greer, *Phys. Rev. Lett.* **2008**, *100*, 155502.
[29] J. R. Greer, W. C. Oliver, W. D. Nix, *Acta Mater.* **2005**, *53*, 1821.
[30] J. Y. Kim, J. R. Greer, *Acta Mater.* **2009**, *57*, 5245.
[31] J. R. Greer, J. T. M. De Hosson, *Prog. Mater. Sci.* **2011**, *56*, 654.
[32] M. C. Liu, J. C. Huang, H. S. Chou, Y. H. Lai, C. J. Lee, T. G. Nieh, *Scripta Mater.* **2009**, *61*, 840.
[33] P. A. Ciullo, N. Hewitt, *The Rubber Formulary*, William Andrew Publishing, Norwich, NY **1999**, p. 55.
[34] K. Dahmen, D. Ertas, Y. Ben-Zion, *Phys. Rev. E* **1998**, *58*, 1494.
[35] K. A. Dahmen, Y. Ben-Zion, J. T. Uhl, *Phys. Rev. Lett.* **2009**, *102*, 175501.
[36] K. A. Dahmen, Y. Ben-Zion, J. T. Uhl, *Nat. Phys.* **2011**, *7*, 554.